Extraction of coherent clusters and grid adaptation in particle-laden turbulence using wavelet filters

Maxime Bassenne,[1,*] Javier Urzay,[1] Kai Schneider,[2] and Parviz Moin[1]

[1]*Center for Turbulence Research, Stanford University, Stanford, California 94305-3024, USA*
[2]*I2M-CNRS, Centre de Mathématiques et d'Informatique, Aix-Marseille Université Marseille, France*

In this study, a wavelet-based method for extraction of clusters of inertial particles in turbulent flows is presented that is based on decomposing Eulerian particle-number-density fields into the sum of coherent (organized) and incoherent (disorganized) components. The coherent component is associated with the clusters and is extracted by filtering the wavelet-transformed particle-number-density field based on an energy threshold. The method is applied to direct numerical simulations of homogeneous-isotropic turbulence laden with small Lagrangian particles. The analysis shows that in regimes where the preferential concentration is important, the coherent component representing the clusters can be described by just 1.6% of the total number of wavelet coefficients, thereby illustrating the sparsity of the particle-number-density field. On the other hand, the incoherent portion is visually structureless and much less correlated than the coherent one. An application of the method, motivated by particle-laden radiative-heat-transfer simulations, is illustrated in the form of a grid-adaptation algorithm that results in nonuniform meshes with fine and coarse elements near and away from particle clusters, respectively. In regimes where preferential concentration in clusters is important, the grid adaptation leads to a significant reduction of the number of control volumes by one to two orders of magnitude.

I. INTRODUCTION

The preferential concentration of inertial particles by turbulent flows is a physical phenomenon often observed in natural and industrial systems. The interaction of particles with turbulence leads to nonuniform spatial distribution of particles resulting from their accumulation in clusters [1]. These clusters influence the engineering performance of a broad range of industrial systems such as liquid-fueled combustors [2] and particle-based solar collectors [3,4]. Specifically, particle clustering influences the transfer of momentum [5,6] and thermal energy [7]. Although the particles accumulate in structures that are easily discernible from visualizations of simulations and experiments, mathematical techniques for the quantitative identification of clusters are rarely reported partly because of the lack of an unequivocal definition of a cluster that would lend itself to an efficient mathematical extraction algorithm. For instance, the reader is referred to Refs. [8,9] for reviews of the state-of-the-art methods for quantifying preferential concentration and particle clusters.

In this study, a technique is proposed to identify clusters of particles in turbulent flows, associating the presence of a cluster with that of local coherence in the particle-number-density field. The method, which is referred to as coherent cluster extraction (CCE) in the notation, is based on wavelet filtering of the number-density field computed from direct numerical simulations (DNS) of Lagrangian inertial particles laden in one-way-coupled, incompressible homogeneous-isotropic turbulence. The results include application of the CCE method in the form of a grid-adaptation algorithm that renders nonuniform meshes clustered around particle clouds. The CCE method is analogous to the coherent vortex extraction method used in earlier works on single-phase turbulent flows to identify coherent

---

*Corresponding author: bassenne@stanford.edu

structures in the vorticity field [10]. However, some important differences arise here with respect to the latter that are highlighted below.

The remainder of this paper is organized as follows. The CCE method is described in Sec. II. The computational setup is outlined in Sec. III. An analysis of the characteristics of the decomposed particle-number-density fields is reported in Sec. IV. The grid-adaptation algorithm is presented in Sec. V along with motivating factors related to particle-laden radiative-heat-transfer simulations. Lastly, conclusions are provided in Sec. VI. An Appendix is included that treats the influences of the particle grid resolution and mean number density.

II. WAVELET-BASED METHOD OF EXTRACTION OF COHERENT PARTICLE CLUSTERS

The CCE method relies on nonlinear wavelet thresholding of the wavelet coefficients of the number-density field $n(\boldsymbol{x},t)$, where $\boldsymbol{x}$ and t denote spatial and time coordinates, respectively. It consists of the following steps: (1) estimation of the particle-number-density field, (2) computation of its wavelet transform, (3) filtering of the number density in wavelet space, and (4) inverse wavelet transformation of the filtered number-density field. These four steps are explained below.

A. Step 1: Estimation of the particle-number-density field

The particle-number-density field n, which is an Eulerian quantity, is a necessary input to the CCE method. However, the discrete particle positions are the only quantities available when the dispersed phase is computed using a Lagrangian formulation, as done in this study and illustrated in Fig. 1(a). A suitable estimate of n based on discrete particle positions is therefore required. Several methodologies for number-density estimation are available that find extensive applications in the astrophysics and plasma physics literature [11–13]. Nonetheless, it is unclear to date whether a universal estimation method for n exists, since each method yields different spectral responses particularly at high wavenumber (e.g., see Fig. 4 in Ref. [13]). In Eulerian treatments of the dispersed phase, the solution to moments of a Boltzmann master equation adapted to macroscopic particles naturally provides the spatiotemporal evolution of the number-density field [14]. However, Eulerian formulations rely on assumptions of an oftentimes unrealistically large number of particles within each homogenized elementary volume. Additionally, the integration of the master equation in turbulent flows, where trajectory crossing may result in singularities of the moment equations, is not exempt from modeling choices that can lead to significantly different distributions of n [15].

In this study, n is estimated by simply projecting the Lagrangian particles onto the nearest-neighbor point of the same grid used to solve the carrier-phase hydrodynamics. A snapshot of the resulting number-density field is shown in Fig. 1(b), which has a strong visual resemblance to the corresponding discrete particle distribution in Fig. 1(a). Comparisons of the results presented here with those obtained using different particle-number-density estimation methods are deferred to future work.

The number of particles N_p is chosen such that the mean number density is $n_0 = \langle n \rangle = N_p/(N\Delta)^3 = 5/\Delta^3$, where $\langle \cdot \rangle$ denotes spatial averaging, N is the number of grid points per direction, and Δ is the grid spacing. If the particles were randomly distributed in space, the ratio of the mean interparticle volume to the grid cell volume would be of order $1/5$, which would lead to a reasonably homogenized description of the particle concentration. However, turbulence alters the distribution of particles by preferentially concentrating them in clusters and creating regions in the flow that are devoid of particles as a result of the locally high values of vorticity [16]. These regions are typically much larger than the mean interparticle distance, as can be observed in Figs. 1(a) and 1(b). Therefore, even if N_p is large enough to warrant a homogenized description in a hypothetical state where the particles are randomly distributed in space, hydrodynamic effects invariably come into play that segregate the particles and degrade the homogenized character of the dispersed phase.

A plausible, yet erroneous approach to palliate this issue and increase the number of particles per homogenized elementary volume would be to increase the homogenization length by coarsening the
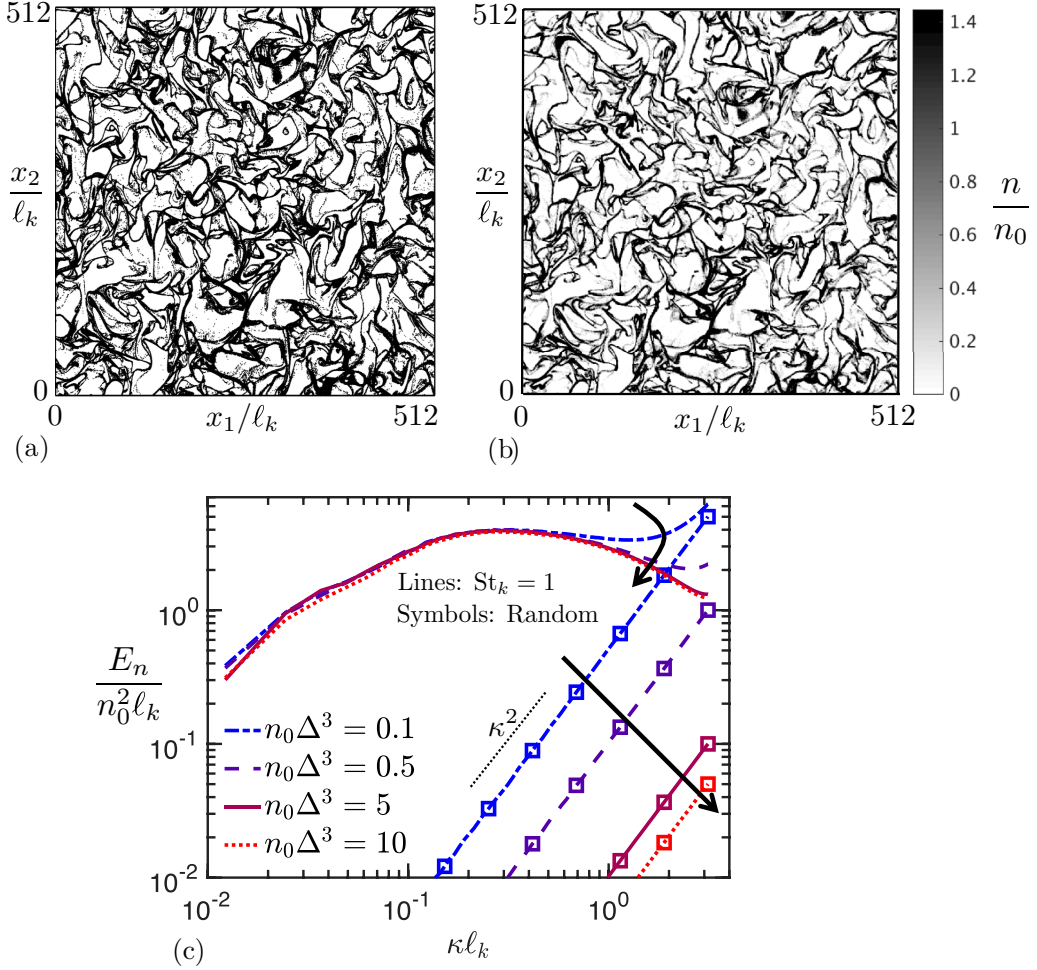
FIG. 1. (a) Instantaneous spatial distribution of particles (dots) contained in a x_3 slice of thickness equal to one Kolmogorov length ℓ_k and (b) corresponding slice of the particle-number-density field, both panels computed for particles with Stokes number $St_k = 1$. Also shown are (c) spherically averaged Fourier energy spectra of the number-density fluctuations obtained from an artificially imposed, random spatial distribution particles (lines with symbols), and from preferentially concentrated particles obtained from DNS (lines). The arrows indicate the variations of the curves with increasing number of particles. Further details of the computational setup are given in Sec. III.

grid used for projection up to scales larger than the size of the hydrodynamically created regions devoid of particles. This would be detrimental for the statistics of the resulting number-density field, whose clusters, which are induced by the small eddies in the present configuration, would be hidden in the subgrid scales, thereby leading to an artificially smoothed spatial distribution of particles. Conversely, if the grid used for projection is refined down to scales similar to the interparticle distance within the clusters, the number-density field would display a checkerboard pattern in those regions that would lead to short-wavelength unphysical noise. This indicates that n is a scale-dependent quantity that in principle depends on the grid employed for projection. There is, however, a compromise between the two aforementioned limiting situations in which the number-density field does not show significant variability with respect to that grid. Such condition

simultaneously involves two requirements for the projection grid, namely, that the grid resolution is comparable to the characteristic hydrodynamic scales responsible for the clustering dynamics and that the grid spacing is larger than the minimum interparticle distance within the clusters.

Closely related to the considerations given above, an additional aspect worthy of discussion is the effect of varying the number of particles in the computation of n. This is illustrated in Fig. 1(c), which shows the effects on the radial Fourier energy spectra of the number-density fluctuations E_n obtained from an artificially imposed, random spatial distribution of particles that follows a Poisson probability distribution function (PDF) with mean and variance equal to n_0 and from a distribution of preferentially concentrated particles computed using DNS of particle-laden homogeneous-isotropic turbulence (see Sec. III for details about the computational setup). The Fourier spectrum can be interpreted as a decomposition of the total particle-number-density field variance into single radial wavenumber contributions. Specifically, Fig. 1(c) shows that, as N_p (or equivalently, n_0) is decreased, the high-wavenumber range of E_n increasingly resembles that of a random distribution of particles with the same mean n_0. This behavior is an artifact caused by the lack of a sufficient number of particles, which introduces short-wavelength noise in n. As a result, N_p must be large enough to ensure that the numerical noise induced by the finite number of particles is much less energetic than the fluctuations of n associated with the hydrodynamic mechanisms that cause the accumulation. The attainment of this limit is illustrated in Fig. 1(c). For $n_0 = 0.1/\Delta^3$, which corresponds to small N_p, the numerical noise is responsible for 80% of the value of the spectrum at small scales. That percentage drops to 50% when $n_0 = 0.5/\Delta^3$ and becomes negligible when $n_0 = 5/\Delta^3$, the latter being the nominal condition used in the present study. Specifically, for $n_0 = 5/\Delta^3$, the relative contribution to E_n from the numerical noise resulting from spatially binning the particles is negligible at this Stokes number. It is worth noting that the aforementioned requirement that the number of particles be large enough so that the induced numerical noise is negligible is desired in the present study since one objective is to obtain physical insights about particle clustering, although in principle it is not necessary for achieving the target decomposition described in Sec. II C. Further considerations about possible effects caused by an insufficient number of particles on results obtained from the CCE method are provided in Sec. IV and the Appendix.

B. Step 2: Wavelet transformation of the particle-number-density field

The wavelet transform of n is given by

$$\check{n}^{(s,d)}(\boldsymbol{x}_s) = \langle n(\boldsymbol{x})\psi^{(s,d)}(\boldsymbol{x} - \boldsymbol{x}_s)\rangle, \tag{1}$$

where $\psi^{(s,d)}(\boldsymbol{x} - \boldsymbol{x}_s)$ are wavelet basis functions that are here taken to be tensor products of orthonormal one-dimensional Coifman-12 wavelets with four vanishing moments, commonly used for wavelet-based studies of turbulent flows [10,17]. The results and conclusions presented below do not change significantly when a lower-order wavelet such as Haar is used (results not shown here for brevity). The time coordinate t has been omitted for brevity in the formulation above. A fast periodic wavelet multiresolution transform algorithm is employed to compute the $N^3 - 1$ discrete wavelet coefficients $\check{n}^{(s,d)}$ [18]. For in-depth explanations of wavelet methods and details regarding the rationale behind choosing a wavelet family, the reader is referred to Refs. [10,17,19–21].

In Eq. (1), $s = (1, 2, \ldots, S)$ are scale exponents, with $S = \log_2 N$ being the number of resolution levels allowed by the grid. The rest of the notation includes $\boldsymbol{x}_s = 2^{s-1}(i\Delta, j\Delta, k\Delta)$, which is a scale-dependent wavelet grid of $(N/2^s)^3$ elements where the wavelets are centered, with $\{i, j, k\} = (1, 3, 5, \ldots, N/2^{s-1} - 1)$ and Δ the grid size, along with a wavelet-directionality index $d = (1, 2, \ldots, 7)$. Wavelets can be ascribed to a representative wavenumber

$$\kappa = \kappa_0 2^{-s} 2\pi/\Delta, \tag{2}$$

where $\kappa_0 = 0.77$ is the normalized centroid wavenumber of the Coifman-12 wavelet. Using Eq. (2), the wavenumber κ and the scale exponent s can be conveniently interchanged.

C. Step 3: Filtering of the particle-number-density field in wavelet space

In analogy to the coherent-vortex-extraction technique proposed in Ref. [10], the CCE method decomposes n as

$$n = n_C + n_I, \tag{3}$$

where n_C and n_I correspond to the coherent and incoherent components, respectively. By construction, these two components are not spatially cross-correlated, as implied by the orthogonality of the wavelets and by the filtering operation described below. The coherent component n_C is related to sufficiently energetic spectral modes of n and can be obtained by using wavelet filtering in the following manner. In their work, Donoho and Johnstone [22] described a wavelet-based algorithm that is optimal for achieving the target decomposition, since it minimizes the maximum $\mathbb{L}^2$-estimation error of n_C. In the present notation, their work implies that the best estimate for n_C is obtained by retaining only the wavelet coefficients $\check{n}^{(s,d)}$ whose absolute values satisfy

$$\check{n}_C^{(s,d)}(\boldsymbol{x}_s) = \begin{cases} \check{n}^{(s,d)}(\boldsymbol{x}_s) & \text{if } |\check{n}^{(s,d)}(\boldsymbol{x}_s)| \geqslant T, \\ 0 & \text{otherwise,} \end{cases} \tag{4}$$

for all scales s, positions $\boldsymbol{x}_s$, and directions d. In Eq. (4), T is a threshold defined as

$$T = \sqrt{2\sigma_{n_I}^2 \ln N^3}, \tag{5}$$

which is written in terms of the unknown variance $\sigma_{n_I}^2$ of the incoherent component n_I. For Eq. (5) to hold, the incoherent component must be assumed to be additive, white, and Gaussian [22]. In this study, the iterative method of Azzalini *et al.* [23] is employed, which converges to T starting from a first iteration where $\sigma_{n_I}^2$ in Eq. (5) is substituted by the variance σ_n^2 of the total field n. The iterative method is deemed as converged when the relative variation in the estimated threshold T is less than 0.1% across consecutive iterations. A maximum of ten iterations were required to obtain the results presented below. This iterative procedure does not introduce any significant computational overhead, since only one wavelet transform is required independently of the number of iterations.

Note that the energy-based, spatially local filter outlined above is fundamentally different from Fourier-based spectral filtering, in that the latter is a scale-sharp filter that acts globally in physical space and does not allow the discrimination of localized, energetic structures. Additionally, unlike Fourier-based filters, the present method does not require periodicity.

D. Step 4: Inverse wavelet transformation of the filtered number-density field

Once the wavelet coefficients of the coherent component of the particle-number-density field are computed, as described above, its physical-space representation is obtained by the inverse wavelet transform

$$n_C(\boldsymbol{x}) = n_0 + \sum_{s=1}^{S} \sum_{\boldsymbol{x}_s} \sum_{d=1}^{7} \check{n}_C^{(s,d)}(\boldsymbol{x}_s)\psi^{(s,d)}(\boldsymbol{x} - \boldsymbol{x}_s). \tag{6}$$

The incoherent portion is readily obtained from Eq. (3) as the difference between n and n_C. This definition of the coherent field is analogous to that of the incoherent component of the vorticity in the technique of coherent vortex extraction in turbulent flows [10]. Further discussions about the implications of the present definition are provided in Sec. IV. In the remainder of this article, the steps 1–4 explained above are illustrated in decomposing number-density fields obtained from DNS of particle-laden turbulence.

III. COMPUTATIONAL SETUP

The linearly forced Navier-Stokes (NS) equations

$$\frac{\partial u_i}{\partial x_i} = 0, \quad \frac{\partial u_i}{\partial t} + u_j \frac{\partial u_i}{\partial x_j} = -\frac{1}{\rho}\frac{\partial p}{\partial x_i} + \nu \frac{\partial^2 u_i}{\partial x_j \partial x_j} + A u_i, \tag{7}$$

are integrated numerically for the carrier phase in a triply periodic cubic domain of side length $L = N\Delta$, where ρ is the density, ν is the kinematic viscosity, p is the hydrodynamic pressure, and u_i denotes velocity components. The explicit form of the forcing coefficient A is provided in a separate study (see Eq. (10) in Ref. [24]). In particular, the forcing yields a constant turbulent dissipation $\epsilon = \langle \nu(\partial u_i/\partial x_j)(\partial u_i/\partial x_j)\rangle$ equal to an imposed value ϵ_∞. This forcing method leads to small temporal fluctuations of the turbulence spectra in the high-wavenumber range [24].

The Lagrangian formulation of the dispersed phase consists of the trajectory equation

$$\frac{dx_{p,i}}{dt} = u_{p,i} \tag{8}$$

for the particle position $x_{p,i}$, where the particle velocity $u_{p,i}$ is obtained from the equation of motion

$$\frac{4}{3}\pi \rho_p a^3 \frac{du_{p,i}}{dt} = 6\pi \rho \nu a(u_i - u_{p,i}), \tag{9}$$

where u_i is the local fluid velocity obtained from a trilinear interpolation at the particle position. In this formulation, the dispersed phase is assumed to be composed of small particles of diameter $2a \ll \ell_k$ and density $\rho_p \gg \rho$, where $\ell_k = (\nu^3/\epsilon_\infty)^{1/4}$ is the Kolmogorov length.

Equations (7)–(9) are solved using an energy-conserving finite-difference formulation with second-order central spatial discretizations and fourth-order Runge-Kutta time integration [25]. The input parameters are $L = 2\pi$, $\nu = 0.05$ and $\epsilon_\infty = 5.6 \times 10^3$, all quantities being expressed in arbitrary yet consistent units leading to a Taylor-Reynolds number $\text{Re}_\lambda = 81$. The calculations are conducted on a staggered, uniform Cartesian grid of $N^3 = 512^3$ points, which translates into a resolution $\kappa_{\max}\ell_k = \pi$, where $\kappa_{\max} = \pi/\Delta$ is the largest resolved wavenumber. Note that with this grid resolution the effective homogenization length for computing the particle-number-density field equals the Kolmogorov length, $\Delta = \ell_k$. After the turbulence has reached a statistically steady state, $N_p = 5N^3 \sim 670$ million monodisperse inertial particles are randomly seeded according to a Poisson distribution under kinematic equilibrium with the carrier phase. The resulting mean number density is $n_0 = 5/\Delta^3$. After sufficiently long times compared to the particle acceleration time $t_a = (2/9)(\rho_p/\rho)(a^2/\nu)$ have passed, 10 solution snapshots are recorded for ensemble averaging during a period $15t_\ell$, where $t_\ell = (2k_\infty/3)/\epsilon_\infty$ is the integral time based on the mean kinetic energy $k_\infty = \langle u_i u_i/2\rangle$.

In addition to the Taylor-Reynolds number, the solution of the problem depends on the Stokes number

$$\text{St}_k = t_a/t_k, \tag{10}$$

where $t_k = \ell_k^2/\nu$ is the Kolmogorov eddy-turnover time. Results are provided below that consider Stokes numbers in the range 0.1–40, with $\text{St}_k \sim 1$ leading to maximum preferential-concentration effects.

IV. NUMERICAL RESULTS

Instantaneous, three-dimensional, and planar projections of the total, coherent, and incoherent components of the particle-number-density resulting from the CCE method are shown in Fig. 2 for $\text{St}_k = 1$. The preferential-concentration effect is clearly visible in the left panel in the form of ligament-like structures characterized by large number-density values. The coherent component shown in the center panel remarkably resembles the same shape and density of structures with
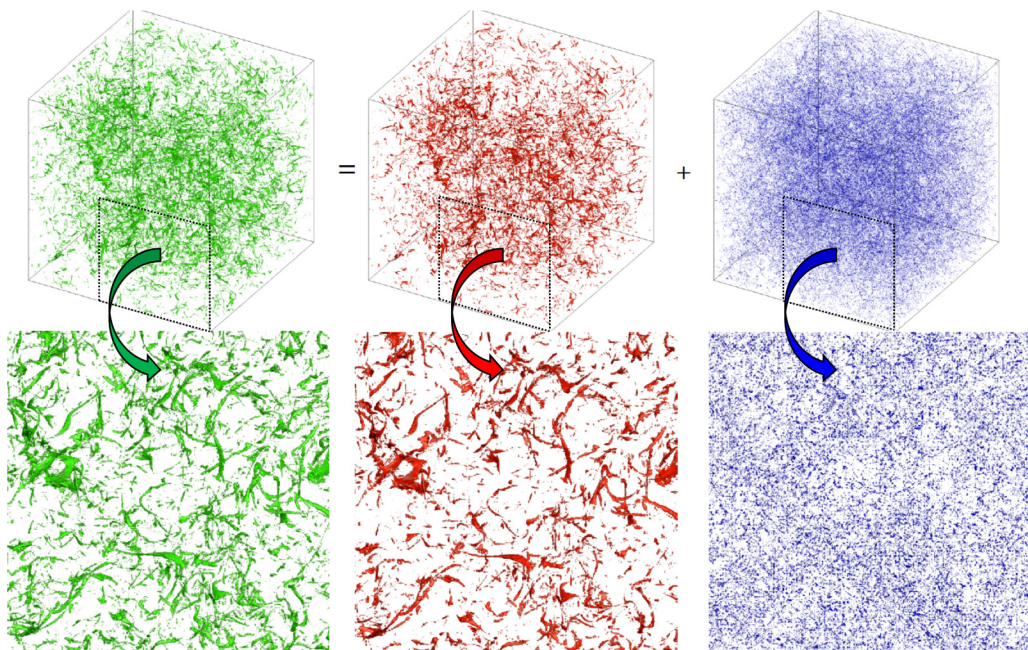
FIG. 2. Instantaneous isosurfaces of total (left), coherent (center), and incoherent (right) components of the particle-number-density field for $St_k = 1$. The values of the isosurfaces are $n = 7\sigma_n$, $n_C = 7\sigma_{n_C}$, and $n_I = (7/3)\sigma_{n_I}$. The upper panel shows three-dimensional views of the entire computational domain. The lower panels show the corresponding 2D projections along the square domain denoted by dashed lines in the upper panels.

slightly sharper edges. On the contrary, the incoherent component of the number density leads to indiscernible structures. The incoherent field homogeneously fills the entire physical domain and does not show significant spatial correlation.

The qualitative visual inspection of the decomposed number-density field made in Fig. 2 suggests that its spatial structure is well captured by the coherent portion. Remarkably, the total compression ratio, defined as the number of nonzero wavelet coefficients N_C of the coherent portion divided by the total number of wavelet coefficients $N^3 - 1$, is always smaller than 1.6%, as shown in Fig. 3(a). This illustrates the sparsity of the particle-number-density field, in that its structures are well represented by very few wavelet coefficients, even in the regime $St_k \sim 1$, where the compression ratio is maximum as a result of the increased coherence enabled by the preferential-concentration effect. This regime requires the largest number of wavelet coefficients to adequately represent the spatially intermittent organization of particles in coherent clusters [see also Fig. 4(b) and discussion associated with flatness values below]. Additionally, Fig. 3(a) includes a sensitivity analysis to the number of particles N_p for $St_k = 1$. If N_p is not sufficiently large, the particle-number-density field exhibits small-scale fluctuations that result in a spatially delocalized unphysical numerical noise, thereby resulting in a decrease of the total compression ratio [see also Fig. 1(c) and discussion in Sec. II A]. As N_p is increased, the compression ratio is observed to converge to 1.6%.

The scale repartition of the compression ratio is provided in Fig. 3(b), which shows the variations with the wavenumber of the ratio of the number of nonzero wavelet coefficients $N_{C,s}$ that contribute to the coherent number-density field at a given scale, to the total number of wavelet coefficients $N_s = 7(N/2^s)^3$ at that scale. The depth of penetration of the coherent component into the small scales is maximum at $St_k = 1$, thus suggesting an increasing degree of small-scale organization in the number-density field in conditions where the preferential-concentration effects are important.
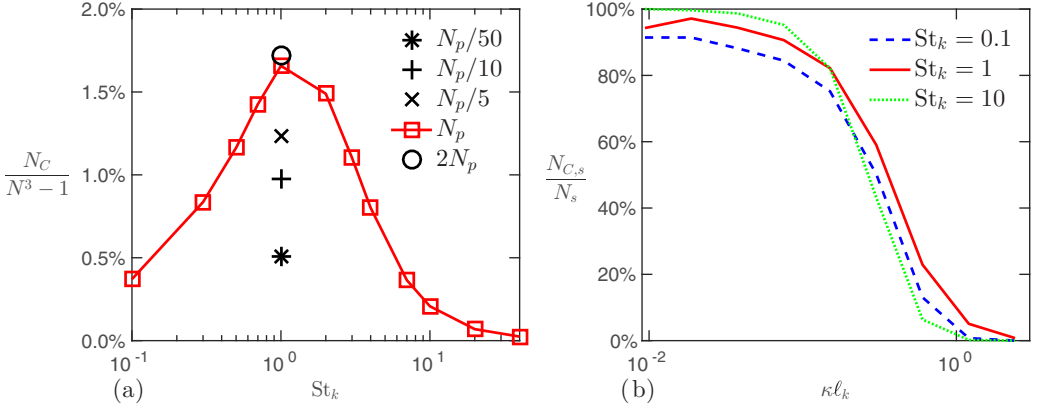
FIG. 3. (a) Global and (b) scale-dependent compression ratios of the total, coherent, and incoherent components of the particle-number-density field.

The second and fourth moments of the PDFs of the total, coherent, and incoherent components of the particle-number-density field are provided in Fig. 4 as a function of the Stokes number. Because of the orthogonality property of the wavelets, the sum of the variances of the coherent ($\sigma_{n_C}^2$) and incoherent ($\sigma_{n_I}^2$) components equals the variance of the total field (σ_n^2). The variance of the coherent field, which is equivalent to the cumulative sum of the corresponding spectral fluctuation energy shown in Fig. 5, represents 80% of the total one at order-unity Stokes numbers and decreases rapidly at smaller or larger Stokes numbers. In those extrema, the incoherent component prevails, as suggested from the intuitive fact that the particles are much less preferentially concentrated. The total number density exhibits maximum flatness under preferential concentration as shown in Fig. 4(b). This result is consistent with the observation that in that regime the particles predominantly interact with intermittent small-scale vortical and straining motions. However, the coherent portion displays slightly larger flatness factors than the total number-density field, which finds visual justification in the slightly sharper edges of the n_C structures shown in Fig. 2 as a result of this filtering approach.
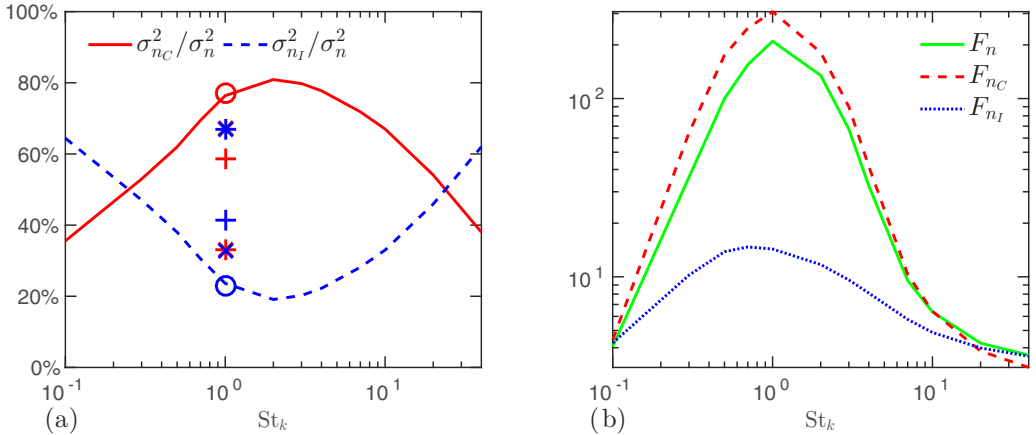

FIG. 4. (a) Relative contributions of the coherent and incoherent particle-number-density fields to the total variance. The legend for the symbols is the same as in Fig. 3. (b) Flatness factor of the total, coherent, and incoherent particle-number-density fields.
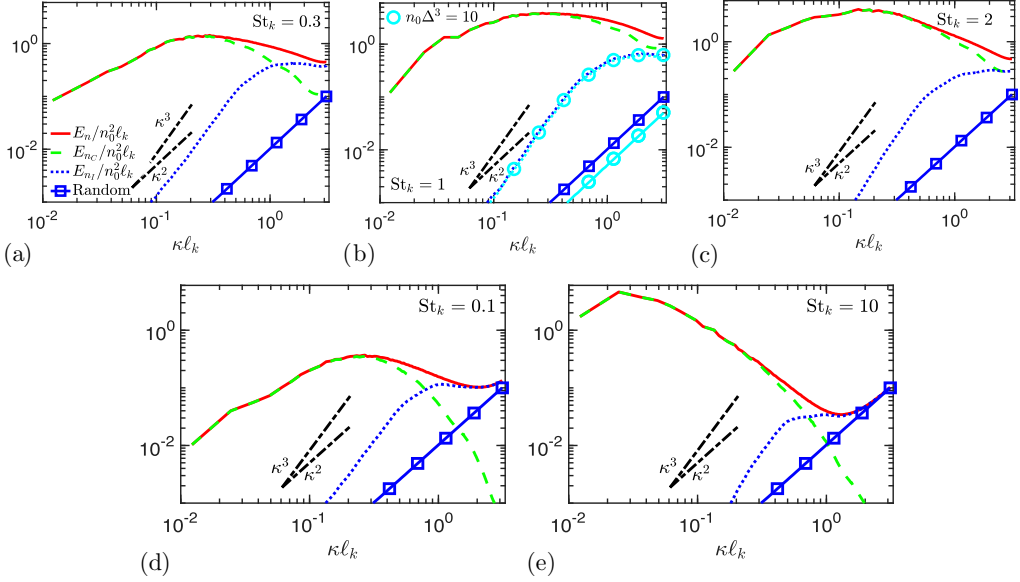
FIG. 5. Fourier energy spectra of the total, coherent, and incoherent particle-number-density fields for (a) $St_k = 0.3$, (b) $St_k = 1$, (c) $St_k = 2$, (d) $St_k = 0.1$, and (e) $St_k = 10$. The solid lines with symbols correspond to a random distribution of particles with the same mean n_0. In Fig. 5(b), the circles correspond to $n_0\Delta^3 = 10$, while all other curves correspond to $n_0\Delta^3 = 5$.

The spectral characteristics of each component of the particle-number-density field are shown in Fig. 5 in terms of the Fourier energy spectra of their fluctuations. In all cases, the spectra of the coherent component tends to follow those of the total field until a Stokes-number-dependent wavenumber beyond which a faster decay is observed in the coherent portion, which ceases to be energetic at the smallest scales due to the lack of clear spatial organization of the particles. Similarly to the observations made on Fig. 3(b) for the scale-dependent compression ratio, the spectral energy associated with the coherent component increasingly pervades the high-wavenumber range and remains energetically relevant there as the preferential concentration regime $St_k \sim 1$ is approached, as shown in Fig. 5(b). In regimes where preferential concentration is not as important, the coherent component becomes energetically irrelevant in the small scales while the incoherent portion does the opposite, as observed in Figs. 5(a), 5(d), and 5(e). In all cases, the slope of the spectra of the incoherent component is not far from 2, which corresponds to that of white noise as prescribed by the equipartition of energy between all wavenumber. This is consistent with the observation made in Fig. 2 that the incoherent number density is visually structureless. However, it should be noted that the slope, which in actuality is closer to 3, shows that the incoherent number density is not entirely decorrelated. This is in contrast with results obtained when the present method is applied to turbulent vorticity fields where the slope of the incoherent-component spectra is sometimes best approximated by 2, although similar cubic slopes such as the one described above can be found in that context depending on the source (see, for instance, Fig. 1 in Ref. [10]).

The exact origin of the incoherent component has no straightforward explanation, since it can be significantly influenced by the short-wavelength noise caused by an insufficient number of particles. To understand this, consider first the cases $St_k = 0.1$ and 10, shown in Figs. 5(d) and 5(e). In those, the upturn in the spectra of the total component of n at high wavenumber is caused by the incoherent one, which is much more energetic than the coherent portion there. However, the spectra of the incoherent component are observed to collapse on those of a random distribution, thus resembling the same characteristics of the artificial noise analyzed in Sec. II A and Fig. 1(c), which is caused by the insufficient number of particles. Since a decrease in N_p shifts upward the random-distribution

spectra, the incoherent portion in Figs. 5(d) and 5(e) would be expected to follow that upward shift and become increasingly energetic in the high-wavenumber range. The opposite trend is expected when N_p is increased, in such a way that the coherent component could be ascribed to a filtered noise-free number density that would have been obtained if a larger number of particles were used [11,26,27]. In all cases, the collapse of the spectra of the incoherent component on the random-distribution spectra occurs only near the maximum grid wavenumber, while the incoherent portion remains more energetic than the random distribution everywhere else. In principle, no clear physical origin can be ascribed to the incoherent part with the number of particles N_p used to obtain these results. However, additional calculations provided in the Appendix at lower Reynolds numbers, which enabled the incrementation of N_p with a reasonable computational cost, indicate that the incoherent portion at $St_k = 0.1$ saturates and does not vanish as N_p is increased (i.e., see top-right panel in Fig. 8), thereby suggesting that this component of the number density may bear some of the small-scale flow randomness when the particles are quasitracers.

At intermediate Stokes numbers, as in Figs. 5(a)–5(c), no clear upturns are observed in the energy spectra of the total number density, with the random-distribution spectra remaining much smaller at the nominal condition $n_0 = 5/\Delta^3$. In these conditions, the spectrum of the incoherent portion is insensitive to doubling the number of particles, as shown in Fig. 5(b). In contradistinction, the random-distribution spectrum is shifted downward if the number of particles is doubled. These observations suggest that, at intermediate Stokes numbers, the incoherent portion might have a physical origin related to the intrinsic lack of organization at small scales as a result of the finite inertia of the particles.

The results described here show that a coherent component of the particle-number-density field can be extracted using wavelet filters and that this component bears structurally the clusters caused by preferential concentration. On the other hand, an incoherent component can be isolated that at intermediate Stokes numbers becomes mostly insensitive to the number of particles and that suggests a certain degree of randomness in the small-scale particle concentration caused by the interaction with the hydrodynamics. The same conclusion is obtained in the Appendix at small Stokes numbers when a larger number of particle is used in a lower Reynolds-number flow. Conversely, the incoherent portion bears mostly numerical noise when the amount of particles seeded in the flow is small.

Based on these observations, there are some restrictive aspects of this work that are absent from the study in Ref. [10] on coherent vorticity extraction in single-phase turbulent flows and that deserve further discussion. The first one is the aforementioned influences of the insufficient number of particles in triggering artificial noise that floods the incoherent component of the number density, which represents a shortfall of the CCE method that is germane to the Lagrangian description employed for the dispersed phase. The second aspect is related to the lack of strict positivity of the coherent and incoherent number-density components, as shown in Fig. 6 and directly implied by the formulation in Sec. II C. Wavelets are not strictly positive since they have zero mean and therefore do not guarantee that the filtered physical-space fields remain positive. As a result, the positive intermittent peaks of the number density tend to get intensified in the clusters detected by the coherent component, this being quantitatively illustrated in Fig. 4(b) by the increase of the coherent-component flatness above that of the total number-density field. These positive overshoots are mirrored by unphysical, small negative concentration values in both coherent and incoherent fields in order to satisfy Eq. (3) and preserve the first and second moments of the total number-density PDF. Although clipping may be exercised in order to remove the negative concentrations, this procedure is artificial and and repels the moment conservation properties of this wavelet filtering method. It should, however, be mentioned that it is possible to transform n into a nearly Gaussian variable and filter it using wavelets as done above [11,26,28], but the antitransformed incoherent component becomes spatially correlated with the coherent portion, which makes the meaning of n_I even more unclear (results not shown here for brevity). The third aspect is related to the nearly cubic slope of the spectra of the incoherent number density found in this study, which suggests that this component is not entirely decorrelated even though it appears to be visually structureless. Additional work, including more appropriate characterizations of the incoherent field, are required
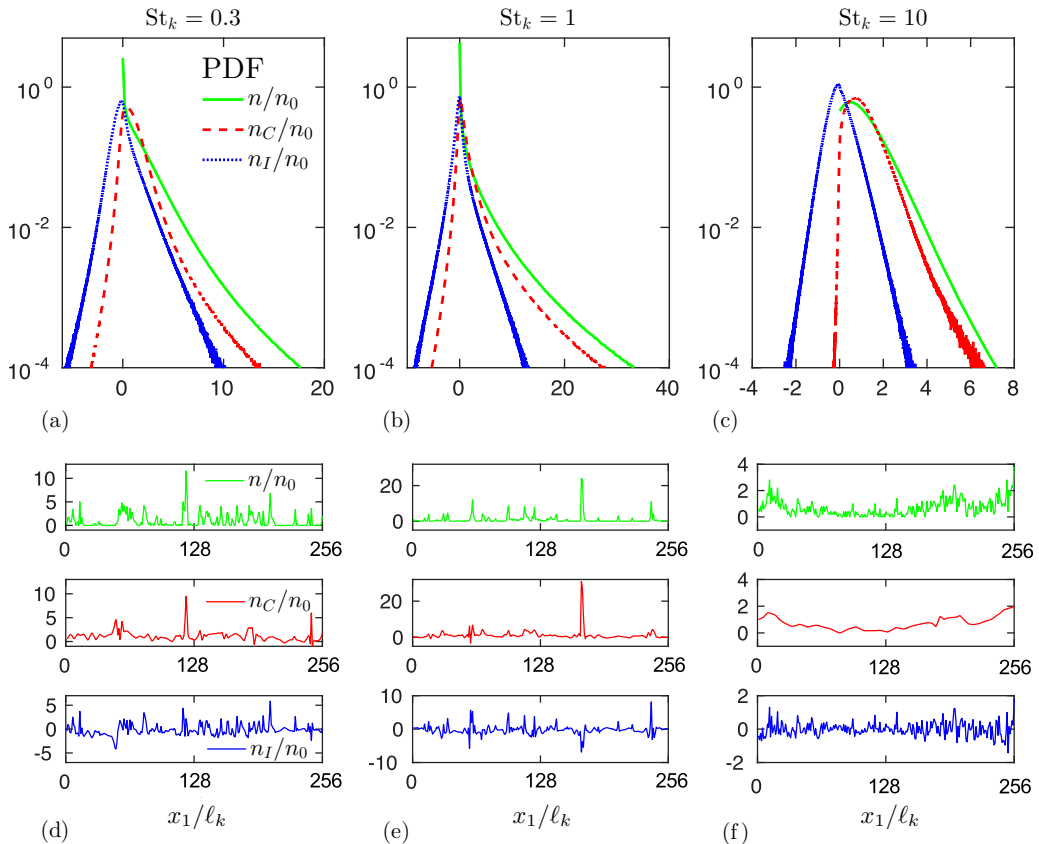
FIG. 6. [(a)–(c)] Ensemble-averaged PDFs of the total, coherent, and incoherent particle number-density fields. [(d), (e)] Corresponding instantaneous one-dimensional profiles of number density along the intersection of the planes $x_2 = L/2$ and $x_3 = L/2$.

to clarify these issues. Special emphasis should be made on the fact that the grid adaptation algorithm formulated in Sec. V does not suffer from the limitations described above, since it does not require antitransformation of the coherent and incoherent wavelet components into physical space.

V. WAVELET-BASED GRID ADAPTATION AROUND PARTICLE CLUSTERS

In this section, the steps 1–3 of the CCE method described in Secs. II A–C are used in the form of a grid-adaptation algorithm. The result is a grid adapted around the clusters of particles, with control volumes being refined there down to scales where the particles cease to be organized.

A. Grid-adaptation algorithm

This algorithm works as follows. The number density field n is first wavelet transformed as described in Sec. II B. Note that large wavelet coefficients are associated with large fluctuations within the corresponding control volume of the scale-dependent wavelet grid x_s, these being markers of underlying coherent (organized) structures within their control volumes. As an illustration, the wavelet coefficients of a one-dimensional version of n are schematically represented in Fig. 7(a) in a scale (s) versus position (x_s) binary tree discretized using 16 collocation points (note that in three dimensions the binary tree becomes an octree). The tagged elements of the tree, which are denoted
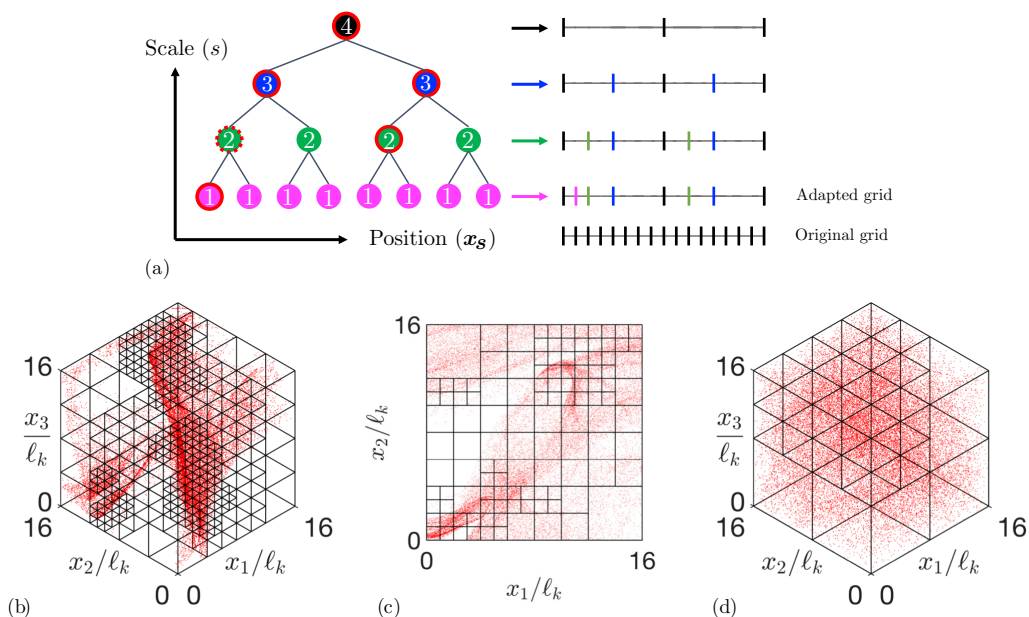
FIG. 7. (a) Schematics of the grid adaptation algorithm using a binary tree for a signal with 16 collocation points (left panel), along with the resulting adapted grid (right panel). Examples of adapted grids obtained by applying the current algorithm to DNS of particle-laden turbulence at [(b), (c)] $St_k = 1$ and (d) $St_k = 10$. The panels show a 1/32th of the total spatial extension of the adapted grid.

by solid red lines, correspond to those with absolute values larger than the threshold T described in Sec. II C, and therefore correspond to the coherent component of n.

In the three-dimensional, practical case, tagging is applied if at least one of the 7 wavelet coefficients of n per location is larger than the threshold. Additional tagging by dashed red lines is done to wavelet coefficients that are smaller than the threshold T but which correspond to a spatial region that contains at least one tagged wavelet coefficient at smaller scales. This tagging procedure ensures that even if particles are randomly distributed at a given scale s but not at a smaller scale $s - 1$, the wavelet coefficient corresponding to scale s at that location will be tagged, therefore triggering local grid refinement at level s.

Starting from the coarsest possible wavelet grid $x_s = x_S$ that contains just one control volume, this algorithm adapts the grid in the following manner. If the wavelet coefficient corresponding to a control volume has been tagged, then that control volume is split into two control volumes, which locally refines the grid. The algorithm is stopped otherwise. The same recursive loop is then applied to the refined control volumes. The final configuration of the adapted computational grid is obtained when either none of the wavelet coefficients in any the control volumes are tagged (i.e., none of the wavelet coefficients belong to the coherent component of n) or the same resolution as the one used in the grid for computing the carrier-phase hydrodynamics is reached [see right-side panel in Fig. 7(a) for a schematics of a grid-adaptation sequence].

The results obtained from this algorithm are illustrated in Figs. 7(b)–7(d), which show visualizations of portions of grids adapted using DNS snapshots of particle-number-density fields using the same numerical setup as described in Sec. III. For the case $St_k = 1$, in which preferential concentration is important, the adapted grid is highly nonuniform and clustered around the particle clouds, where the maximum resolution given by the reference grid used to solve the carrier-phase hydrodynamics is attained. The grid elements are much coarser in regions where the particle concentration is lower. Remarkably, the adapted grid has 12 million elements, which corresponds to 8.9% of the total number of control volumes of the reference grid. By way of contrast, utilization

of this algorithm for the case $St_k = 10$ leads to a coarser and more uniform grid since there is no significant particle clustering. In this case, the adapted grid has 1 million elements, which corresponds to 0.7% of the total number of control volumes of the reference grid. In the present study, the threshold was set exactly to the theoretical value described in Sec. II C, although there are no obstacles for relaxing this constraint and varying it depending on the target accuracy of the radiation solver. Analyses of the impact of the choice of the threshold value on the accuracy of the numerical discretization of commonly encountered physical conservation equations on the adapted grid will be the subject of future work.

B. Potential applications

The utilization of adapted grids resulting from this algorithm may be of some interest for relieving the computational cost of a number of multiphase flow problems that involve physical processes that predominantly occur near particle clusters, such as interphase coupling effects, since the adaptation procedure benefits from the fast $O(N^3)$ wavelet-transform algorithm [18]. For instance, one of these problems could be the phenomenon of autoignition of fuel sprays, which tends to develop in fuel-droplet clouds [2,29].

Another problem of interest for this grid-adaptation algorithm, which lays within the overarching context of solar-power receivers [3,4], is that of a gas laden with solid particles receiving thermal radiation from a hot external source. Specifically, the numerical solution of this problem involves integration of the radiative heat-transfer equation, whose formulation involves the local values of the spectral emissivity, absorptivity, and scattering coefficients. For a transparent fluid laden with a large number of randomly dispersed small particles, the absorptivity coefficient is given by $\sigma_a(\boldsymbol{x}) = n(\boldsymbol{x})A_p$ in each control volume, with $A_p = \pi a^2$ as the particle cross-sectional area. However, in the presence of clouds of preferentially concentrated particles, the numerical solution of the radiative transfer equation subject to the above approximation provides inaccurate values of the radiation-intensity attenuation partly because the particles are no longer randomly distributed [30,31]. The requirement of randomness in the particle spatial distribution, which is necessary for using the above closure of the absorptivity coefficient, poses a strong constraint on the grid resolution employed to solve the constitutive equations of radiation transport. In a preferentially concentrated field of particles, such as the one shown in Fig. 1(a), a random distribution within each control volume would only be recovered when the projection grid is sufficiently fine. The underlying reason for this limitation is that preferential concentration is induced by small-scale turbulence structures in the types of homogeneous flows addressed here. One alternative is to use a coarse grid along with a subgrid-scale model that accounts for the subgrid clustering of particles. A different approach, which does not require modeling, is to use the CCE method to dynamically identify and locate the presence of clusters and nonuniformly adapt the grid with the algorithm described above, in such a way that the resulting distribution of particles is random within all grid cells. The corresponding number density n for the computation of σ_a is then computed by projecting the particles on the adapted grid.

The approach described here is reminiscent of existing wavelet-optimized adaptive methods based on vorticity—rather than particle concentration—wavelet coefficients that trigger local mesh refinement around eddies in single-phase flows [21]. An aspect worthy of further investigation is the quantification of the extent to which the coherent fields of vorticity and number density may be related in particle-laden turbulent flows.

VI. SUMMARY AND CONCLUSIONS

This study presents a method for coherent cluster extraction (CCE) that decomposes an Eulerian particle-number-density field into the sum of a coherent (organized) and an incoherent (disorganized) components. The coherent component is computed using wavelet filtering. The incoherent component is defined as the remainder. The CCE method is applied to snapshots

of number-density fields obtained from DNS of homogeneous-isotropic turbulence laden with Lagrangian inertial particles. The coherent component structurally bears the clusters of particles at a strikingly low compression ratio of 1.6%, indicating that the number-density field is extremely sparse in regimes where preferential concentration prevails. On the contrary, the incoherent component tends to homogeneously fill the space and visually shows no clear structure, even though a detailed analysis of its spectrum suggests some degree of spatial correlation, as revealed by a nearly cubic slope.

An application of the CCE method is illustrated in the form of a grid-adaptation algorithm, which results in nonuniform grids whose cells contain none of the significant fluctuations of the number density encountered in clustered clouds, in such a way that the particles within each control volume follow an approximate random spatial distribution. This, for instance, is one of the conditions required for the validity of simplifying assumptions of the radiative-transfer equation that oftentimes finds difficult justification in turbulent flows laden with absorbing particles that preferentially concentrate in clusters. The adaptation algorithm reduces the grid size by one to two orders of magnitude.

The present study deals with homogeneous-isotropic turbulence, which favors the use of periodic boundary conditions. However, as mentioned in Sec. II C, periodicity is not required in the CCE method. This could motivate, for instance, the characterization of particle clusters in turbulent channel flows [32].

APPENDIX: INFLUENCES OF THE PARTICLE GRID RESOLUTION AND MEAN NUMBER DENSITY

This Appendix addresses the effects of varying the mean number density of particles n_0 and the resolution of the grid employed to project the particles and create the Eulerian field n. The resolution of the projection grid is denoted here by the symbol Δ_p, as opposed to Δ, which represents the DNS grid spacing. In order to vary these characteristic parameters by two orders of magnitude around their nominal values $n_0\Delta^3 = O(10)$ and $\Delta_p/\Delta = 1$ while keeping the flow resolution at $\kappa_{max}\ell_k = \pi$ and limiting the computational cost, a setup similar to that described in Sec. III is employed but subject to a smaller Taylor-Reynolds number $\mathrm{Re}_\lambda = 49$ instead. The corresponding input parameters are $L = 2\pi$, $\nu = 0.05$, and $\epsilon_\infty = 3.5 \times 10^2$. The reference grid used to solve the conservation equations has 256^3 elements. Three classes of particles with $\mathrm{St}_k = 0.1$, 1, and 10 are considered. The mean number of particles per computational volume is varied from $n_0\Delta^3 = 0.8$ to $n_0\Delta^3 = 80$, the latter corresponding to approximately $N_p = 1.3$ billion particles. Particle-number-density fields are computed on a uniform Cartesian grid with grid resolution Δ_p ranging from $\Delta/2$ to 2Δ.

Table I reports the resulting global compression ratio for different values of Δ_p and mean number densities. In all cases, the compression ratio increases as the number of particles is increased. This is a signature of the decrease in the relative contribution of the numerical noise caused by the finite number of particles to the incoherent wavelet coefficients, which results in an increased number of coherent wavelet coefficients. Note, however, that the rate of increase of the compression ratio decreases with increasing number of particles, thereby suggesting that the compression ratio may be converging to a small number independent of it. As observed for the $\mathrm{St}_k = 1$ case, the more coherent the total number-density field is, the smaller is the proportional change in the compression ratio as the number of particles is varied. This is in contrast to the large or small Stokes number cases, whose number-density fields have smaller fluctuation energies at small scales and therefore require a larger number of particles to devise any signs of probable convergence. For $\mathrm{St}_k = 0.1$ and 10, the compression ratio decreases with decreasing Δ_p, since that is equivalent to adding a noisy signal

TABLE I. Effects of the particle projection-grid resolution and particle mean number density on the global compression ratio in percentage.

$N_C/(N^3 - 1) \times 100$	$St_k = 0.1$			$St_k = 1$			$St_k = 10$		
Δ_p/Δ $\qquad$ $n_0\Delta^3$	0.8	8	80	0.8	8	80	0.8	8	80
2.0	0.40	0.89	1.02	1.29	1.42	1.43	0.38	1.24	1.96
1.0	0.09	0.52	0.97	1.20	1.87	2.01	0.06	0.27	0.95
0.5	0.02	0.13	0.56	0.73	1.61	2.37	0.01	0.04	0.19

caused by the deficit of particles in constructing the Eulerian field. On the other hand, at $St_k = 1$ and $n_0\Delta^3 = 80$, when the number-density spectra appear to be converged (see discussion below), decreasing Δ_p results in an increased compression ratio, although the corresponding increase occurs at a smaller rate than the decrease observed at $St_k = 0.1$ and 10.

The sensitivity of the incoherent number-density component is further investigated by considering the effect of the number of particles on the Fourier energy spectra of the fluctuations of n at a fixed projection-grid resolution $\Delta_p = \Delta$, as shown in Fig. 8. As previously noted in Secs. II and IV, for $St_k = 1$ the spectra become independent of the number of particles when a sufficiently large number
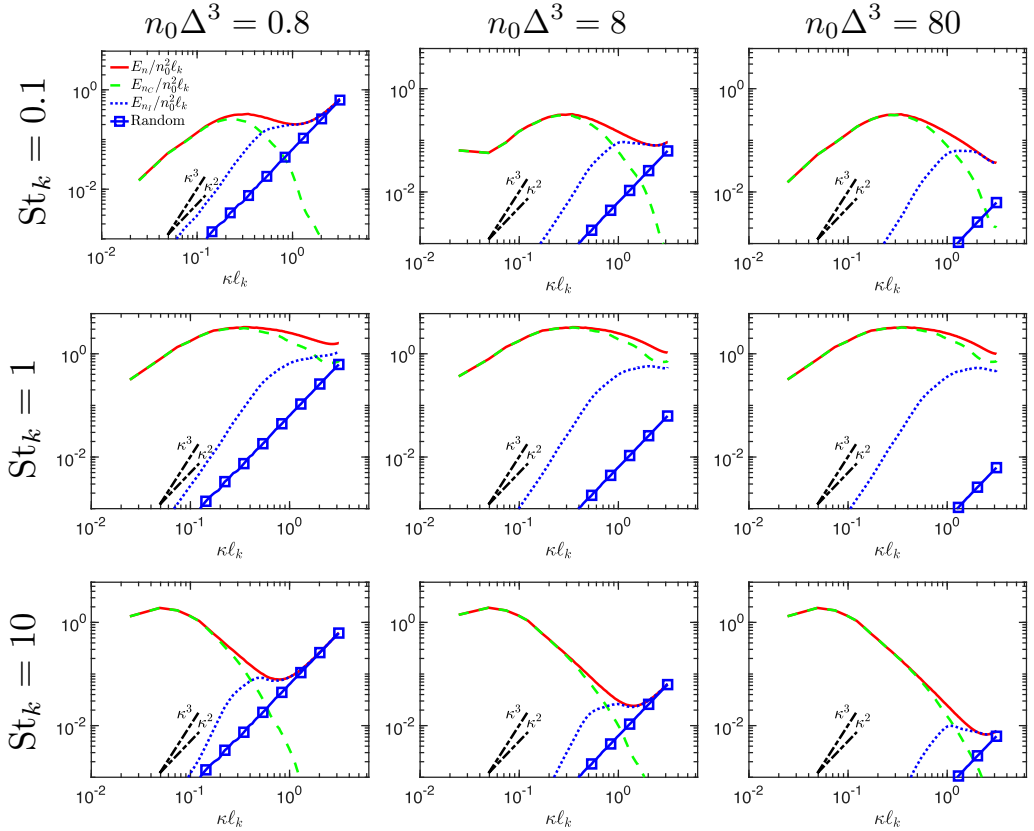

FIG. 8. Effect of the particle mean number density on the Fourier energy spectra of the total, coherent, and incoherent particle-number-density fields for (top row) $St_k = 0.1$, (center row) $St_k = 1$, and (bottom row) $St_k = 10$. The solid lines with symbols correspond to a random distribution of particles with the same mean n_0. The particle grid resolution is $\Delta_p = \Delta$.

of particles is employed. This was shown in Fig. 1(c) for the main computations and in this Appendix in the center row in Fig. 8 for the lower-Re$_\lambda$ simulations. Specifically, the spectra in the center and right panels for St$_k = 1$ in Fig. 8, which correspond to nominal and increased number of particles, respectively, are identical except for the expected downward shift of the spectrum associated with a random distribution of particles, whose contribution to the number-density field is negligible. A similar convergence process is observed for St$_k = 0.1$ in Fig. 8, whereas the large-wavenumber range of the spectra in the case St$_k = 10$ continues to undergo large variations as the number of particles is increased.

[1] S. Balachandar and J. K. Eaton, Turbulent dispersed multiphase flow, Annu. Rev. Fluid Mech. **42**, 111 (2010).

[2] A. L. Sánchez, J. Urzay, and A. Liñán, The role of separation of scales in the description of spray combustion, Proc. Combust. Inst. **35**, 1549 (2015).

[3] M. Rahmani, G. Geraci, G. Iaccarino, and A. Mani, *Polydisperse Particles in an Irradiated Turbulent Gas-Particle Mixture*, Annual Research Briefs 2015, Center for Turbulence Research (Stanford University, Stanford, 2015), pp. 27–41.

[4] H. Pouransari and A. Mani, Effects of preferential concentration on heat transfer in particle-based solar receivers, J. Sol. Energy Eng. **139**, 021008 (2017).

[5] A. Ferrante and S. Elghobashi, On the physical mechanisms of two-way coupling in particle-laden isotropic turbulence, Phys. Fluids **15**, 315 (2003).

[6] D. H. Richter, O. Garcia, and C. Astephen, Particle stresses in dilute, polydisperse, two-way coupled turbulent flows, Phys. Rev. E **93**, 013111 (2016).

[7] A. Frankel, H. Pouransari, F. Coletti, and A. Mani, Settling of heated particles in homogeneous turbulence, J. Fluid Mech. **792**, 869 (2016).

[8] R. Monchaux, M. Bourgoin, and A. Cartellier, Analyzing preferential concentration and clustering of inertial particles in turbulence, Int. J. Multiphase Flow **40**, 1 (2012).

[9] C. Marchioli, Large-eddy simulation of turbulent dispersed flows: A review of modeling approaches, Acta Mech. **228**, 741 (2017).

[10] M. Farge, G. Pellegrino, and K. Schneider, Coherent Vortex Extraction in 3D Turbulent Flows Using Orthogonal Wavelets, Phys. Rev. Lett. **87**, 054501 (2001).

[11] A. B. Romeo, C. Horellou, and J. Bergh, *N*-body simulations with two-orders-of-magnitude higher performance using wavelets, Mon. Not. R. Astron. Soc. **342**, 337 (2003).

[12] B. Terzić and G. Bassi, New density estimation methods for charged particle beams with applications to microbunching instability, Phys. Rev. Spec. Top-Ac **14**, 070701 (2011).

[13] T. Peterka, H. Croubois, N. Li, E. Rangel, and F. Cappello, Self-adaptive density estimation of particle data, SIAM J. Sci. Comput. **38**, S646 (2016).

[14] F. A. Williams, *Combustion Theory* (Benjamin/Cummings, Menlo Park, California, 1985).

[15] D. Kah, A. Vié, C. Chalons, and M. Massot, *Second Order Scheme for Quadrature-Based Velocity High Order Moment Methods for Disperse Two-Phase Flows*, Annual Research Briefs 2011, Center for Turbulence Research (Stanford University, Stanford, 2011), pp. 312–334.

[16] K. D. Squires and J. K. Eaton, Preferential concentration of particles by turbulence, Phys. Fluids **3**, 1169 (1991).

[17] N. Okamoto, K. Yoshimatsu, K. Schneider, M. Farge, and Y. Kaneda, Coherent vortices in high resolution direct numerical simulation of homogeneous isotropic turbulence: A wavelet viewpoint, Phys. Fluids **19**, 115109 (2007).

[18] S. G. Mallat, A theory for multiresolution signal decomposition: The wavelet representation, IEEE T. Pattern Anal. **11**, 674 (1989).

[19] M. Farge and G. Rabreau, Transformée en ondelettes pour détecter et analyser les structures cohérentes dans les écoulements turbulents bidimensionnels, Compt. Rend. Acad. Sci. **307**, 1479 (1988).

[20] C. Meneveau, Analysis of turbulence in the orthonormal wavelet representation, J. Fluid Mech. **232**, 469 (1991).

[21] K. Schneider and O. Vasilyev, Wavelet methods in computational fluid dynamics, Annu. Rev. Fluid Mech. **42**, 473 (2010).

[22] D. L. Donoho and I. M. Johnstone, Ideal spatial adaptation by wavelet shrinkage, Biometrika **81**, 425 (1994).

[23] A. Azzalini, M. Farge, and K. Schneider, Nonlinear wavelet thresholding: A recursive method to determine the optimal denoising threshold, Appl. Comput. Harmon. Anal. **18**, 177 (2005).

[24] M. Bassenne, J. Urzay, G. I. Park, and P. Moin, Constant-energetics physical-space forcing methods for improved convergence to homogeneous-isotropic turbulence with application to particle-laden flows, Phys. Fluids **28**, 035114 (2016).

[25] H. Pouransari, M. Mortazavi, and A. Mani, *Parallel Variable-Density Particle-Laden Turbulence Simulation*, Annual Research Briefs 2015, Center for Turbulence Research (Stanford University, Stanford, 2015), pp. 43–54.

[26] A. B. Romeo, C. Horellou, and J. Bergh, A wavelet add-on code for new-generation *n*-body simulations and data de-noising (jofiluren), Mon. Not. R. Astron. Soc. **354**, 1208 (2004).

[27] R. Nguyen Van Yen, D. del Castillo-Negrete, K. Schneider, M. Farge, and G. Chen, Wavelet-based density estimation for noise reduction in plasma simulations using particles, J. Comput. Phys. **229**, 2821 (2010).

[28] F. J. Anscombe, The transformation of poisson, binomial, and negative-binomial data, Biometrika **35**, 246 (1948).

[29] D. Martínez-Ruiz, J. Urzay, A. L. Sánchez, A. Liñán, and F. A. Williams, Dynamics of thermal ignition of spray flames in mixing layers, J. Fluid Mech. **734**, 387 (2013).

[30] R. A. Shaw, A. B. Kostinski, and D. D Lanterman, Super-exponential extinction of radiation in a negatively correlated random medium, J. Quantum Spectrosc. Radiat. Transfer **75**, 13 (2002).

[31] A. Frankel, G. Iaccarino, and A. Mani, Convergence of the Bouguer-Beer law for radiation extinction in particulate media, J. Quantum Spectrosc. Radiat. Transfer **182**, 45 (2016).

[32] T. Sakurai, K. Yoshimatsu, K. Schneider, M. Farge, K. Morishita, and T. Ishihara, Coherent structure extraction in turbulent channel flow using boundary adapted wavelets, J. Turbulence **18**, 352 (2017).